

Mixed Quantum-Classical Approaches to Spin Current and Polarization Dynamics in Chiral Molecular Junctions

Yu Wang,^{†,‡} Ruihao Bi,^{†,‡} Wei Liu,^{†,‡} Jiayue Han,^{†,‡} and Wenjie Dou^{*,†,‡}

[†]*Department of Chemistry, School of Science, Westlake University, Hangzhou 310024
Zhejiang, China*

[‡]*Institute of Natural Sciences, Westlake Institute for Advanced Study, Hangzhou 310024
Zhejiang, China*

E-mail: douwenjie@westlake.edu.cn

Abstract

Chiral molecular junctions offer a promising platform for realizing chiral-induced spin selectivity (CISS), where spin filtering occurs without external magnetic fields. Here, we investigate spin transport in such junctions by combining quantum master equation (QME) methods for purely electronic dynamics with surface hopping (SH) and mean-field Ehrenfest (MF) approaches to incorporate electron-phonon coupling. Our results show that transient spin polarization arises but ultimately decays to zero at long times. We find that bias voltage, molecular length, and spin-orbit coupling (SOC) strongly influence the spin current dynamics: higher bias enhances spin current but reduces polarization, while longer molecules and stronger SOC amplify transient polarization. Including electron-phonon coupling modifies current-voltage characteristics, enhancing spin currents at intermediate bias but suppressing them at high bias, while leaving the polarization dynamics largely unchanged. These findings highlight

the interplay between electronic and vibrational effects in CISS and provide guidance for designing molecular spintronic devices.

INTRODUCTION

The interplay between molecular chirality and spin-dependent electron transport has garnered significant interest due to the discovery of the Chiral-Induced Spin Selectivity (CISS) effect.¹ This phenomenon, wherein chiral molecules preferentially transmit electrons of a particular spin orientation, challenges conventional understanding of spin polarization, especially in systems composed of light, nonmagnetic elements.² CISS offers a promising route toward molecular spintronics, enabling spin filtering, spin injection, and even magnetoresistance control without relying on magnetic materials or external magnetic fields.^{3–5}

Experimental observations of CISS span a diverse range of chiral systems, including helical peptides,^{6–8} DNA strands,^{9–11} and synthetic helicenes,^{12–14} revealing robust spin polarization effects under both electrical and optical excitations. At the same time, recent experiments on single-molecule junctions have reported no detectable spin polarization, indicating that in the coherent transport regime the probability of a spin-flip transition is less than 10^{-6} , rendering the effect too small to be experimentally observed.¹⁵ These seemingly contrasting results highlight the complexity of CISS and the influence of experimental conditions, such as molecular environment, ensemble effects, and coupling to electrodes. However, the theoretical foundation of CISS remains under active debate. Key challenges include explaining the emergence of significant spin polarization from systems with weak intrinsic spin-orbit coupling (SOC), capturing dynamical effects during electron transport, and understanding the role of electronic coherence and decoherence in molecular junctions.¹⁶

Existing theoretical approaches—ranging from static scattering theory^{17–19} and non-equilibrium Green’s function (NEGF) methods^{20–24} to time-dependent wavepacket dynamics²⁵—have provided valuable insights but often yield inconsistent predictions depending on assumptions about electronic structure, SOC strength, and environmental interactions. Notably, certain models reproduce pronounced spin selectivity, while others, even when applied to similar systems, fail to predict any spin polarization at all.²⁶

In this work, we combine quantum master equation (QME) method for purely electronic

dynamics with surface hopping (SH) and mean-field Ehrenfest (MF) approaches to incorporate electron-phonon coupling, to simulate spin transport for chiral molecule junctions. This framework allows us to capture both coherent spin transport and vibrationally assisted processes in chiral molecular junctions. We adopt the chiral molecular junction model introduced in Ref. 27, which builds on Ref. 28, with the only modification being the replacement of quantum nuclear vibrations by classical ones. We systematically investigate how bias voltage, molecular length, SOC strength, and electron-phonon interactions affect the time-dependent evolution of spin current and spin polarization. Our results show that the spin current increases with stronger bias. Spin polarization appears transiently on the sub-picosecond timescale but always decays to zero at long times. Stronger SOC and longer molecular backbones enhance the magnitude of the transient polarization. Electron-phonon coupling further modifies current-voltage characteristics, enhancing currents at intermediate bias but suppressing them at high bias, while leaving the polarization dynamics largely unaffected. These findings provide new insights into the interplay between SOC and vibrational effects in chiral systems. They highlight the critical role of transient dynamics in understanding spin selectivity and suggest strategies for optimizing spin transport in molecular devices. Our work paves the way for designing chiral molecular junctions with tailored spintronic functionalities and for exploring vibrationally assisted spin control in nanoscale systems.

RESULTS AND DISCUSSIONS

Following Refs. 27 and 28, we consider a chiral molecule as the system, modeled as a helical structure with radius a and pitch c . The spatial coordinates of site m are given by

$$\mathbf{r}_m = (a \cos \phi_m, a \sin \phi_m, (m-1)c/(N-1)), \quad (1)$$

$$\phi_m = 2\pi(m-1)N_{\text{laps}}/(N-1), \quad (2)$$

where $N = N_{\text{laps}} \times N_{\text{ions}}$ is the total number of sites, with N_{laps} denoting the number of helical turns and N_{ions} the number of sites per turn.

The system Hamiltonian follows the chiral molecular model:

$$\begin{aligned} \hat{H}_s = & \sum_{m=1}^N \epsilon_0 \hat{d}_m^\dagger \hat{d}_m + \frac{1}{2} \hbar \omega_0 (\mathbf{R}^2 + \mathbf{P}^2) - \sum_{m=1}^{N-1} \left(\hat{d}_m^\dagger \hat{d}_{m+1} + H.c. \right) \left[t_0 + \sqrt{2} t_1 \mathbf{R}_m \right] \\ & + \sum_{m=1}^{N-2} i \left(\hat{d}_m^\dagger \boldsymbol{\nu}_m^+ \cdot \boldsymbol{\sigma} \hat{d}_{m+2} \right) \left[\lambda_0 + \sqrt{2} \lambda_1 \mathbf{R}_m \right] \end{aligned} \quad (3)$$

The molecular Hamiltonian describes a chiral tight-binding chain of N sites coupled to a single vibrational mode of frequency ω_0 , incorporating both nearest-neighbor electron-phonon interactions and next-nearest-neighbor spin-orbit coupling (SOC). The first term accounts for the on-site electronic energy ϵ_0 at each site, while the second term represents the energy of the classical vibrational mode described by nuclear position \mathbf{R} and momentum \mathbf{P} . The third term captures electron hopping between adjacent sites with amplitude t_0 , which is modulated linearly by the phonon displacement with coupling constant t_1 , thus enabling phonon-assisted charge transfer. The last term introduces an intrinsic SOC between next-nearest neighbors, proportional to $i \boldsymbol{\nu}_m^s \cdot \boldsymbol{\sigma}$, where the unit vector $\boldsymbol{\nu}_m^s = \mathbf{d}_{m+s} \times \mathbf{d}_{m+2s}$ ($s = \pm 1$) encodes the local chirality, with $\mathbf{d}_{m+s} = (\mathbf{r}_m - \mathbf{r}_{m+s})/|\mathbf{r}_m - \mathbf{r}_{m+s}|$. This geometric factor ensures that the SOC strength reflects the handedness of the helical backbone. This SOC is characterized by a bare strength λ_0 and a phonon-modulated contribution λ_1 , allowing the

vibrational mode to dynamically influence spin-dependent transport. Such SOC amplitude is also modulated by the linear phonon displacement.

Additionally, we include the fermionic bath, representing the metal electrodes, along with the system–bath coupling in the total Hamiltonian, which is presented in the Theoretical Framework section.

The parameters used in this paper: $\epsilon_0 = -240$ meV, $\omega_0 = 0.4$ meV, $t_0 = 40$ meV, $t_1 = 4$ meV, $\lambda_0 = 1$ meV (10 meV), $\lambda_1 = 0.1$ meV, $k_B T = 25$ meV. For system-bath coupling $\Gamma_L^A = \Gamma_L(\mathcal{I} + A\sigma_z)$, $\Gamma_L = \Gamma_R = 10$ meV, $A = +(-)\frac{1}{2}$ for spin up (spin down) current. $\mu_L = -\mu_R$, bias voltage $\Phi = (\mu_L - \mu_R)/e$.

WITHOUT NUCLEAR MOTION

We first investigate the spin polarization in the absence of nuclear motion, focusing on the effects of the molecular length and spin–orbit coupling (SOC) strength. The current is calculated using a single-particle quantum master equation (QME) approach.

Figure 1 shows the time-dependent current (left panels) and spin polarization (right panels) for the chiral tight-binding system under different applied voltage biases Φ . Here, we consider a short chiral molecule with $N_{\text{laps}} \times N_{\text{ions}} = 1 \times 5$. Left panels (a, c, e, g) display the spin-resolved currents for spin-up (blue solid line) and spin-down (red dashed line). Right panels (b, d, f, h) show the corresponding spin polarization, defined as $\frac{I_{\uparrow} - I_{\downarrow}}{I_{\uparrow} + I_{\downarrow}} \times 100\%$. In the low-bias regime ($\Phi = 0.1$ V and 0.2 V), the currents are very small, initially negative due to the transient response, and nearly identical for spin-up and spin-down on the picosecond timescale. The spin polarization exhibits large short-time fluctuations (up to $\sim 20\%$) but decays to nearly zero in the long-time steady state. The inset in Fig. 1b and c shows the current and polarization at 100 ps, where the current gradually stabilizes after the initial transient, and the spin polarization, despite strong early fluctuations, ultimately vanishes. At intermediate bias ($\Phi = 0.4$ V), the current increases to the sub-microampere range. The spin polarization shows a sharp transient peak (about 2%), yet it also vanishes in the steady

state. In the high-bias regime ($\Phi = 0.6$ V), the current reaches the microampere scale ($\sim 1.8\text{--}2.0$ μA). The spin polarization is strongly suppressed, showing only a small transient peak ($\sim 0.5\%$) before decaying to zero.

Figure 2 presents the corresponding results for a longer chiral molecule with $N_{\text{laps}} \times N_{\text{ions}} = 2 \times 5$. Similar to Fig. 1, the left panels present the spin-resolved currents for spin-up (blue solid line) and spin-down (red dashed line), while the right panels display the corresponding spin polarization. Compared to the shorter molecule, the overall current amplitude changes only slightly across all bias regimes, indicating that current transport is not strongly affected by the increased length on the timescale considered. In contrast, the transient spin polarization is significantly enhanced. At low bias ($\Phi = 0.1$ V), the polarization exhibits large short-time fluctuations reaching nearly 40%. For $\Phi = 0.2$ V, the transient polarization exceeds 40%. The long-time results (100 ps) shown in the inset of Fig. 2b and c indicate that the polarization decays to nearly zero in the steady state. At intermediate bias ($\Phi = 0.4$ V), the transient polarization is reduced but still reaches about 6%, while at high bias ($\Phi = 0.6$ V) it remains finite at approximately 1%. In all cases, however, the polarization decays to nearly zero in the steady state.

Figure 3 shows the short chiral molecule under different bias voltages Φ with the SOC strength increased by an order of magnitude compared to Fig. 1. The enhancement of SOC leads to a dramatic increase in the transient spin polarization. At low bias ($\Phi = 0.1$ V), the polarization exceeds 100%, arising from the fact that the total current ($I_{\uparrow} + I_{\downarrow}$) approaches zero near the transient crossing point, which amplifies the polarization ratio. When the bias is $\Phi = 0.2$ V, the transient polarization reaches values above 200%. The long-time behavior depicted in the inset of Fig. 3b and c demonstrates that the polarization diminishes to nearly zero in the steady state. At intermediate bias ($\Phi = 0.4$ V), the polarization still shows a sizable transient peak of more than 20%, while at high bias ($\Phi = 0.6$ V) it remains finite at around 4%. In all cases, however, the polarization decays to nearly zero at long times.

Figure 4 presents the results for the long chiral molecule with the SOC strength enhanced

by a factor of ten compared to Fig. 2. With both increased molecular length and stronger SOC, the transient spin polarization is markedly amplified. At low bias ($\Phi = 0.1$ V), the polarization reaches nearly 300%, while at $\Phi = 0.2$ V it approaches 400%. The inset of Fig. 4b and c shows that, at 100 ps, the polarization has essentially decayed to zero, indicating a vanishing steady-state value. At intermediate bias ($\Phi = 0.4$ V), the polarization remains sizable at over 40%, and at high bias ($\Phi = 0.6$ V) it still exceeds 7%. Despite these large transient enhancements, the polarization decays toward zero in the steady state, consistent with the behavior observed in shorter molecules and weaker SOC cases.

These results indicate that, for the chiral tight-binding model considered here, transient spin polarization can be substantial, but the long-time steady-state polarization vanishes in the absence of nuclear motion.

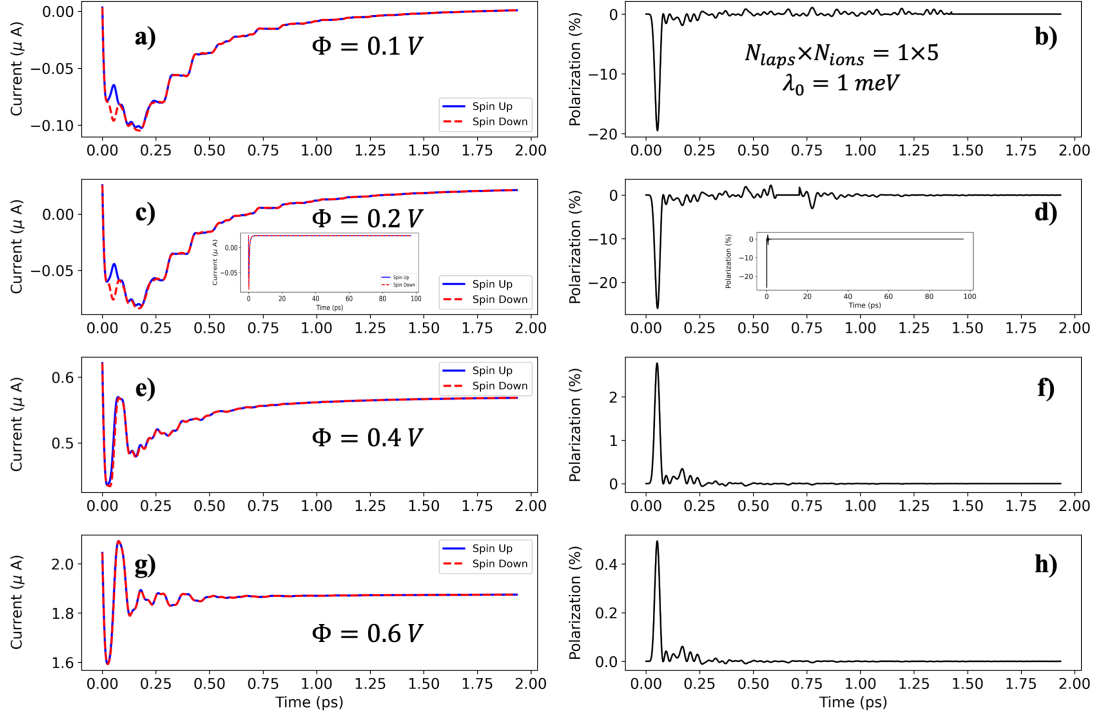


Figure 1: Time-dependent spin current (left panels) and spin polarization (right panels) for a $N_{\text{laps}} \times N_{\text{ions}} = 1 \times 5$ chiral molecule under different biases: (a, b) $\Phi = 0.1$ V, (c, d) $\Phi = 0.2$ V, (e, f) $\Phi = 0.4$ V, and (g, h) $\Phi = 0.6$ V. Here, we applied a small SOC strength where $\lambda_0 = 1$ meV.

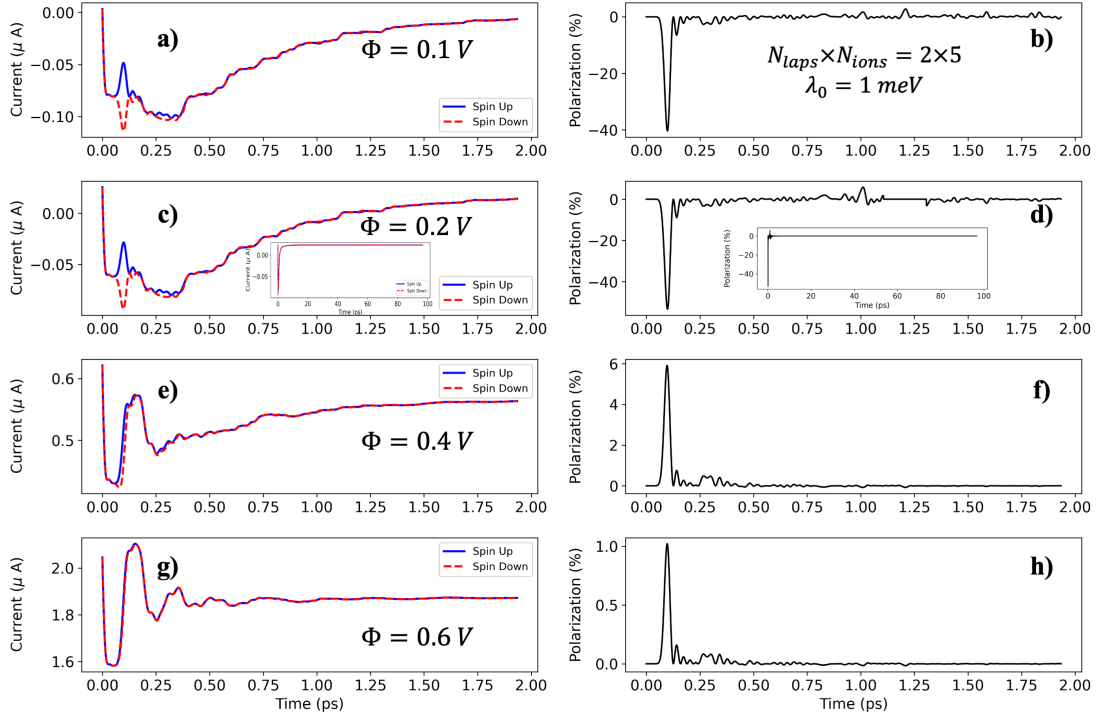


Figure 2: Time-dependent spin current (left panels) and spin polarization (right panels) for a $N_{\text{laps}} \times N_{\text{ions}} = 2 \times 5$ chiral molecule under different biases: (a, b) $\Phi = 0.1 \text{ V}$, (c, d) $\Phi = 0.2 \text{ V}$, (e, f) $\Phi = 0.4 \text{ V}$, and (g, h) $\Phi = 0.6 \text{ V}$. Here, we applied a small SOC strength where $\lambda_0 = 1 \text{ meV}$.

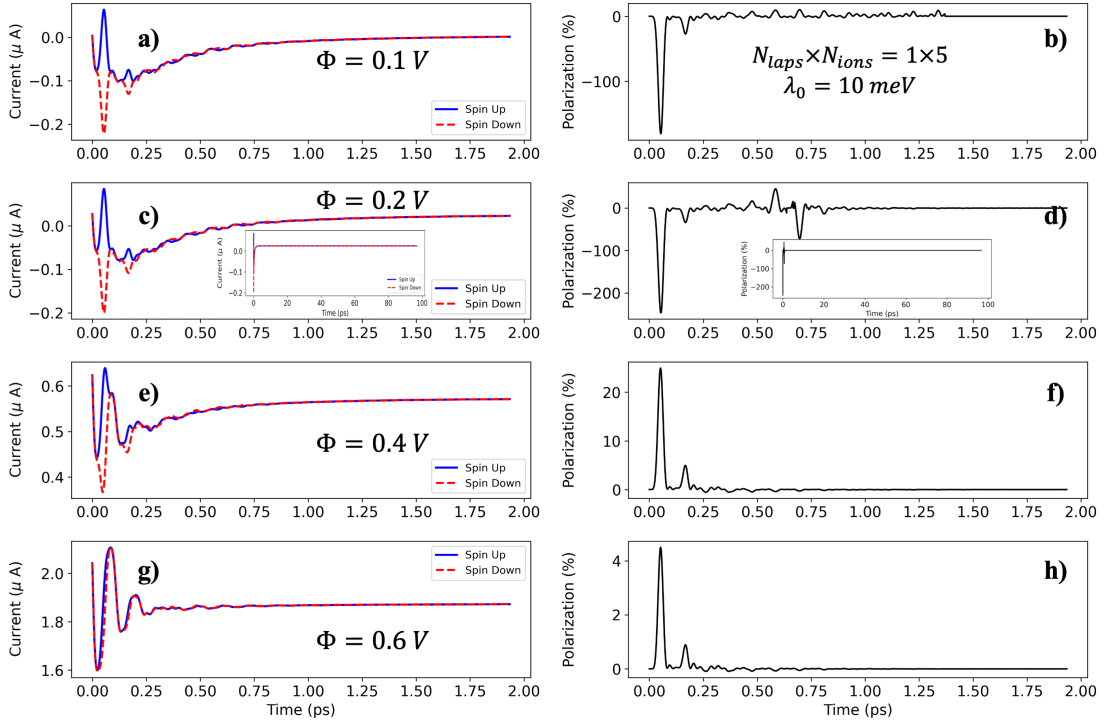


Figure 3: Time-dependent spin current (left panels) and spin polarization (right panels) for a $N_{\text{laps}} \times N_{\text{ions}} = 1 \times 5$ chiral molecule under different biases: (a, b) $\Phi = 0.1 \text{ V}$, (c, d) $\Phi = 0.2 \text{ V}$, (e, f) $\Phi = 0.4 \text{ V}$, and (g, h) $\Phi = 0.6 \text{ V}$. Here, we applied a large SOC strength where $\lambda_0 = 10 \text{ meV}$.

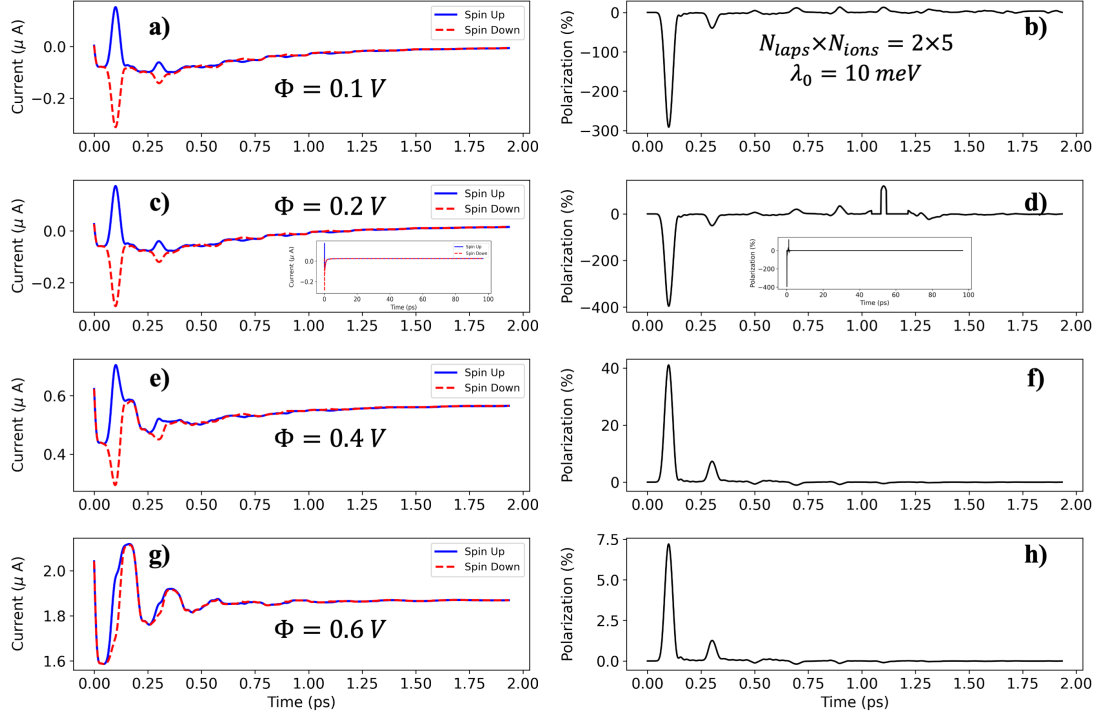


Figure 4: Time-dependent spin current (left panels) and spin polarization (right panels) for a $N_{\text{laps}} \times N_{\text{ions}} = 2 \times 5$ chiral molecule under different biases: (a, b) $\Phi = 0.1 \text{ V}$, (c, d) $\Phi = 0.2 \text{ V}$, (e, f) $\Phi = 0.4 \text{ V}$, and (g, h) $\Phi = 0.6 \text{ V}$. Here, we applied a large SOC strength where $\lambda_0 = 10 \text{ meV}$.

WITH NUCLEAR MOTION

In this section, we introduce electron–phonon coupling into both the nearest-neighbor (NN) hopping and next-nearest-neighbor (NNN) SOC terms. The spin current dynamics are evaluated using the surface hopping (SH) and mean-field Ehrenfest (MF) methods.

In Figure 5, the left panels (a, c, e, g) display the time-dependent spin-resolved currents under different bias voltages Φ , while the right panels (b, d, f, h) show the corresponding spin polarizations. Results obtained from the QME (gray lines) represent the reference case without nuclear motion. The SH (blue/red lines) and MF (green/orange lines) dynamics account for electron–phonon coupling. At low bias ($\Phi = 0.1$ V), the transient spin currents obtained from QME, SH, and MF coincide almost perfectly for the first 2 ps, indicating that in such short chiral molecule, the transient electronic transport is dominated by elastic tunneling. In this regime, the available bias window is too small to activate inelastic phonon channels, so nuclear motion does not play a significant role.

When the bias is increased to $\Phi = 0.2$ V, SH dynamics predicts a modest current enhancement relative to QME, while MF fails to reproduce this effect. The enhancement can be attributed to phonon-assisted tunneling, where electronic transitions couple to vibrational displacements, effectively opening additional inelastic channels.^{29–31} The SH method captures stochastic hopping between adiabatic surfaces, which better describes the phonon-induced broadening of transport channels, whereas MF, being an averaged mean-field approach, underestimates this effect.^{32,33}

At an intermediate bias ($\Phi = 0.4$ V), the role of electron–phonon coupling becomes more pronounced. Both SH and MF yield significantly larger steady-state currents compared to QME. In this regime, the bias window is sufficiently large that multiple inelastic channels open, and phonon scattering facilitates electron flow by effectively broadening the transmission spectrum. This behavior can be viewed as phonon-assisted conduction, where nuclear fluctuations reduce localization effects and increase electronic delocalization along the transport pathway.^{34,35}

At high bias ($\Phi = 0.6$ V), however, electron-phonon coupling suppresses the current relative to QME. In this regime, strong driving enhances electron-phonon scattering, which introduces decoherence and backscattering, thereby reducing the net current. Since the phonon frequency is very small (0.4 meV) compared to the bias, the lattice behaves almost like a classical fluctuating environment; instead of opening new transport channels, these fluctuations primarily act to randomize electronic motion and dissipate current. This explains why the current is lower than in the purely electronic case at large bias.^{36,37}

In contrast to the strong bias-dependent effects on the spin-resolved current, the spin polarization (right panels of Fig. 5) remains essentially unaffected by nuclear motion across all voltages. Both SH and MF reproduce the QME polarization, which shows short-lived transient peaks but vanishes in the long-time steady state.

When the length of the chiral molecule is increased (Fig. 6) or the SOC strength is enhanced (Fig. 7), the overall bias-dependent trends of the spin current remain qualitatively the same as those observed in the short chiral molecule. Specifically, electron-phonon coupling continues to play a negligible role at low bias, enhances current through phonon-assisted tunneling at intermediate bias, and suppresses current due to scattering and decoherence at high bias. For longer molecules, the transient current exhibits stronger amplitude variations and responds more rapidly, showing either enhancement or suppression at earlier times depending on the applied bias voltage (left panels in Fig. 6). With stronger SOC, the ultrafast (fs-scale) variations of the spin current retain the same amplitude as in the case without nuclear motion, while the slower (ps-scale) variations remain unchanged compared to the weak-SOC case for the same molecular length (left panels of Figs. 7 and 8).

Although the ps-scale spin current is influenced by electron-phonon coupling, the spin polarization remains unaffected by nuclear motion across all bias voltages (right panels of Figs. 6 - 8), underscoring that phonon effects alone cannot generate or sustain spin selectivity.

Finally, we perform an 800 ps electronic dynamics simulation on a short chiral molecule with $\lambda_0 = 1$ meV and $\Phi = 0.2$ V, as shown in Fig. 9. Over this long-time evolution,

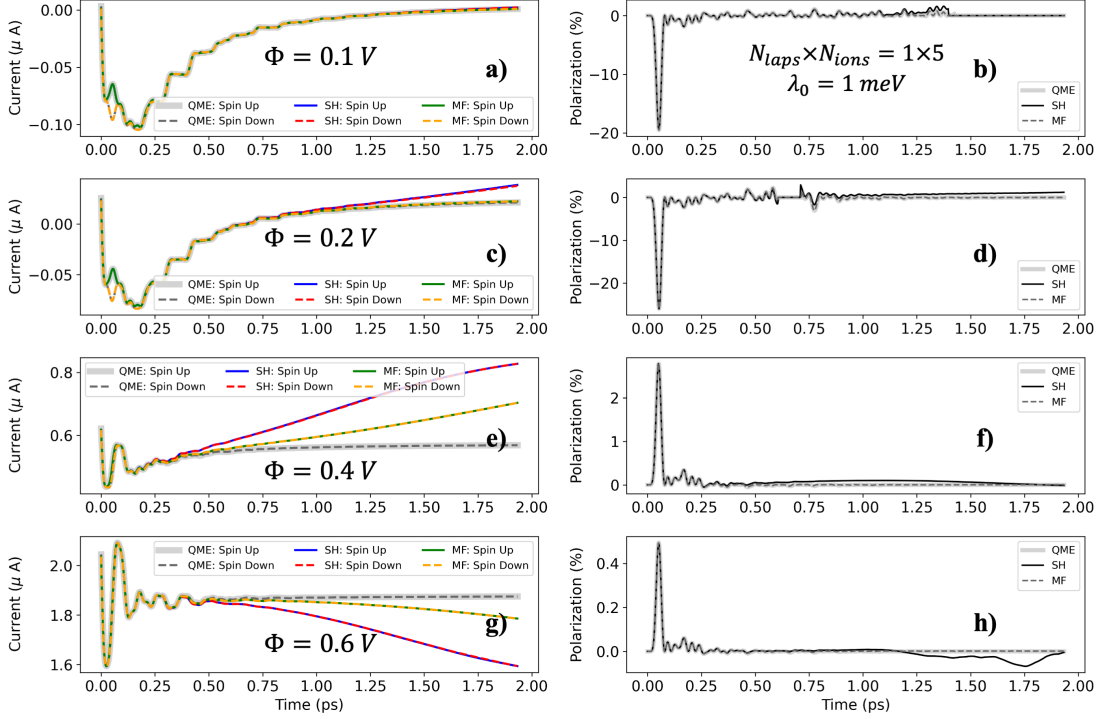


Figure 5: Time-dependent spin current (left panels) and spin polarization (right panels) for a $N_{\text{laps}} \times N_{\text{ions}} = 1 \times 5$ chiral molecule with electron-phonon couplings under different biases: (a, b) $\Phi = 0.1$ V, (c, d) $\Phi = 0.2$ V, (e, f) $\Phi = 0.4$ V, and (g, h) $\Phi = 0.6$ V. Here, we applied a small SOC strength where $\lambda_0 = 1$ meV.

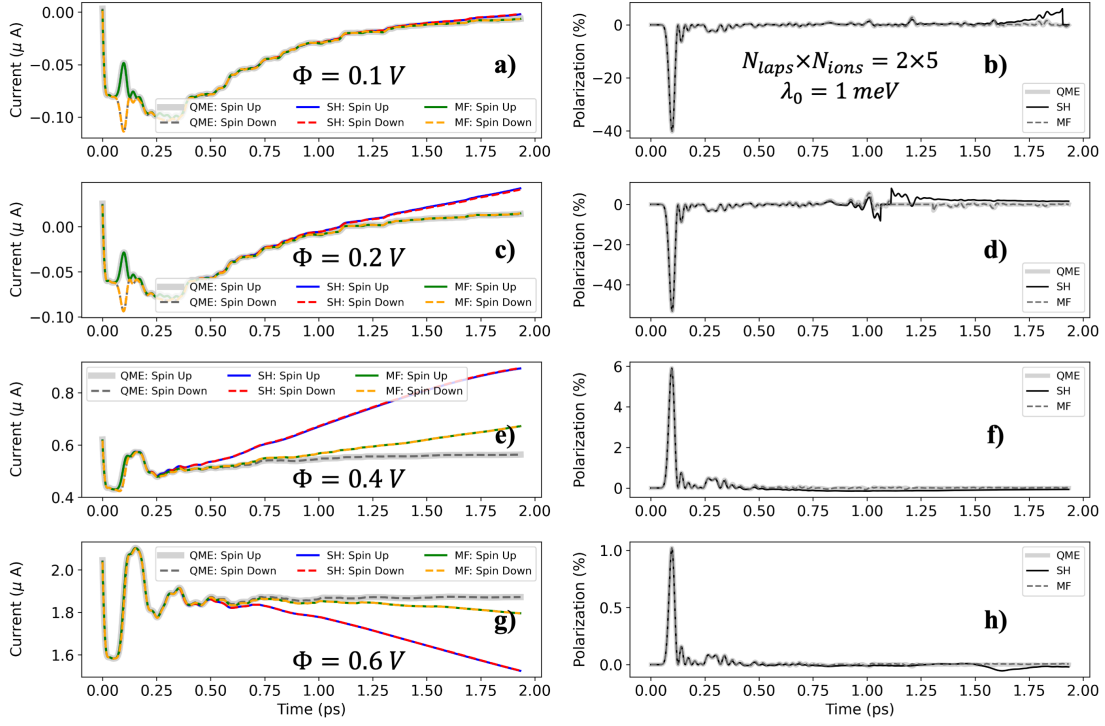


Figure 6: Time-dependent spin current (left panels) and spin polarization (right panels) for a $N_{\text{laps}} \times N_{\text{ions}} = 2 \times 5$ chiral molecule with electron-phonon couplings under different biases: (a, b) $\Phi = 0.1$ V, (c, d) $\Phi = 0.2$ V, (e, f) $\Phi = 0.4$ V, and (g, h) $\Phi = 0.6$ V. Here, we applied a small SOC strength where $\lambda_0 = 1$ meV.

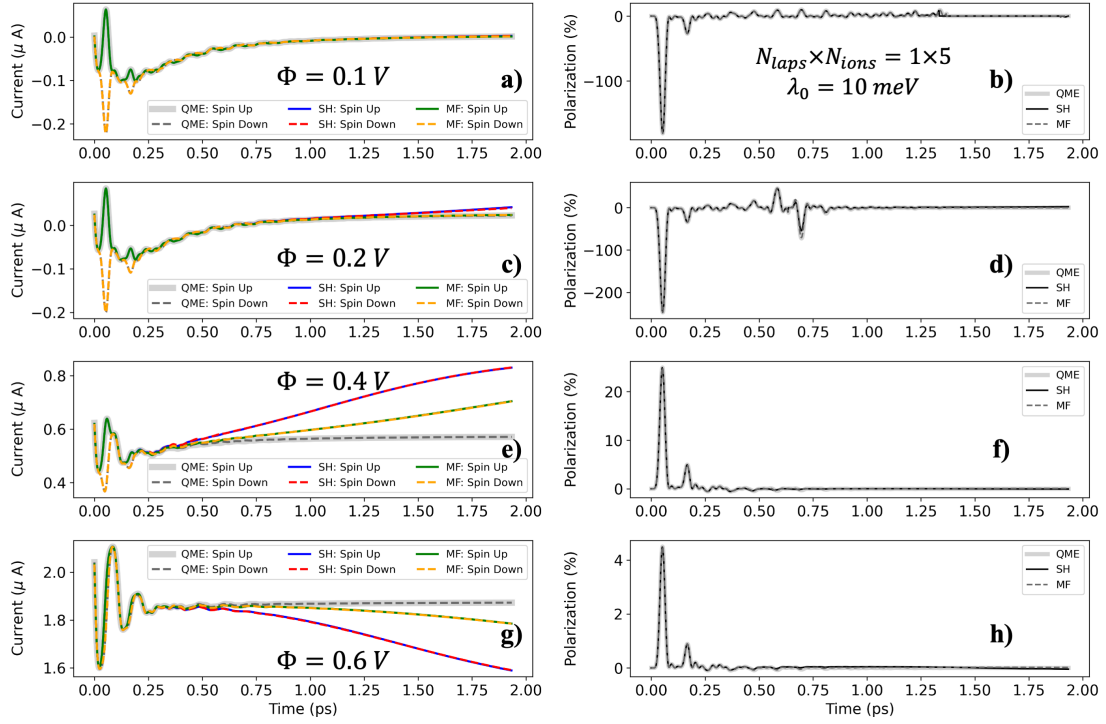


Figure 7: Time-dependent spin current (left panels) and spin polarization (right panels) for a $N_{\text{laps}} \times N_{\text{ions}} = 1 \times 5$ chiral molecule with electron-phonon couplings under different biases: (a, b) $\Phi = 0.1$ V, (c, d) $\Phi = 0.2$ V, (e, f) $\Phi = 0.4$ V, and (g, h) $\Phi = 0.6$ V. Here, we applied a large SOC strength where $\lambda_0 = 10$ meV.

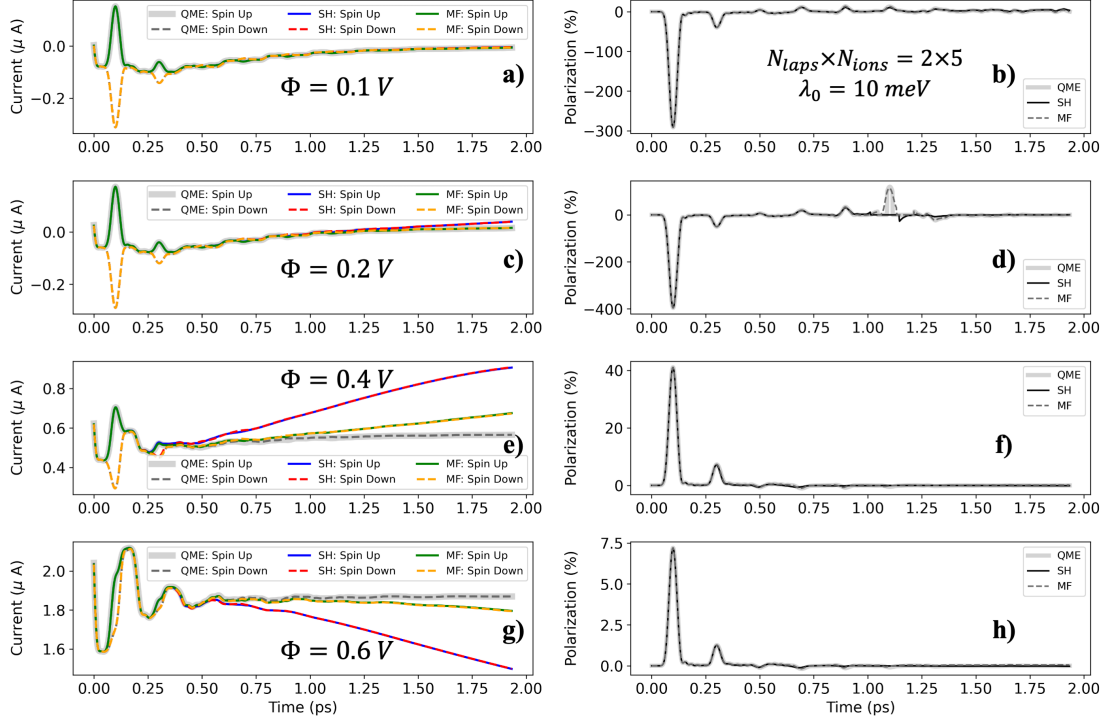


Figure 8: Time-dependent spin current (left panels) and spin polarization (right panels) for a $N_{\text{laps}} \times N_{\text{ions}} = 2 \times 5$ chiral molecule with electron-phonon couplings under different biases: (a, b) $\Phi = 0.1$ V, (c, d) $\Phi = 0.2$ V, (e, f) $\Phi = 0.4$ V, and (g, h) $\Phi = 0.6$ V. Here, we applied a large SOC strength where $\lambda_0 = 10$ meV.

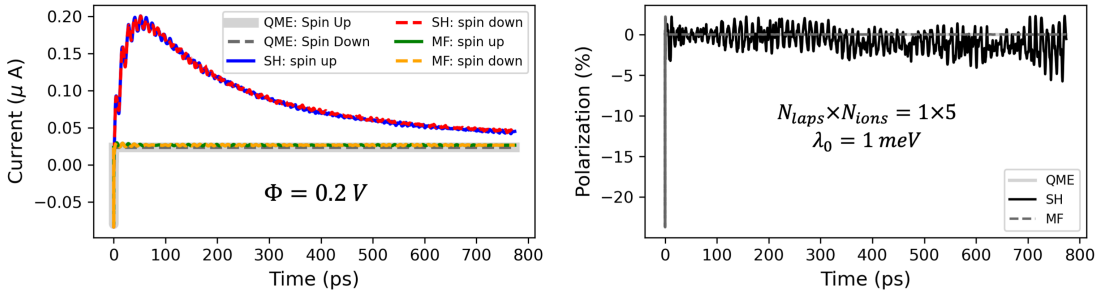


Figure 9: Time-dependent spin current (a) and spin polarization (b) for a $N_{\text{laps}} \times N_{\text{ions}} = 1 \times 5$ chiral molecule with electron-phonon couplings under a bias of $\Phi = 0.2$ V. A small SOC strength of $\lambda_0 = 1$ meV is applied, and the dynamics are evolved for 800 ps.

the spin current obtained from SH initially increases and then decreases relative to QME, whereas MF fails to capture this behavior. The overall spin selectivity from SH results fluctuates around zero, indicating that in this regime electron-phonon coupling does not sustain a robust spin polarization. Instead, phonon-induced scattering primarily acts to randomize the spin-dependent transport pathways, preventing the emergence of significant spin selectivity over extended timescales.

THEORETICAL FRAMEWORK

EQUATION OF MOTION

The general model Hamiltonian in our study consists of three components: the system part (without electron-electron interaction); the bath part; and the system-bath coupling part:

$$\hat{H}_t = \hat{H}_s + \hat{H}_b + \hat{H}_c, \quad (4)$$

$$\hat{H}_s = \sum_{mn} h_{mn}(\mathbf{R}) \hat{d}_m^\dagger \hat{d}_n + U(\mathbf{R}) + T(\mathbf{P}), \quad (5)$$

$$\hat{H}_b = \sum_k \epsilon_k \hat{c}_k^\dagger \hat{c}_k, \quad (6)$$

$$\hat{H}_c = \sum_{kn} V_{kn} (\hat{c}_k^\dagger \hat{d}_n + \hat{d}_n^\dagger \hat{c}_k) \quad (7)$$

It is always possible to transform the one-electron Hamiltonian \hat{h} into the adiabatic representation,

$$\hat{H}_s = \sum_{mn} h_{mn}(\mathbf{R}) \hat{d}_m^\dagger \hat{d}_n + U(\mathbf{R}) + T(\mathbf{P}) \quad (8)$$

$$= \sum_p \tilde{h}_{pp}(\mathbf{R}) \hat{d}_p^\dagger \hat{d}_p + U(\mathbf{R}) + T(\mathbf{P}) \quad (9)$$

where $\hat{d}_p = \sum_m \Lambda_{pm} \hat{d}_m$, with $\hat{\Lambda}$ being a unitary matrix, such that \hat{h} is diagonal, $\sum_{nm} \Lambda_{pn}^\dagger h_{nm} \Lambda_{mq} = \delta_{pq} \tilde{h}_{pq}$. Accordingly, the system-bath coupling Hamiltonian becomes,

$$\hat{H}_c = \sum_{kp} \tilde{V}_{kp} \left(\hat{c}_k^\dagger \hat{d}_p + \hat{d}_p^\dagger \hat{c}_k \right), \quad (10)$$

where $\tilde{V}_{kp} = \sum_m V_{km} \Lambda_{mp}$, so the hybridization function $\tilde{\Gamma}_{pq}$ in the wide band approximation

is,

$$\tilde{\Gamma}_{pq}(\mathbf{R}) = \sum_k \tilde{V}_{kp}^* \tilde{V}_{kq} \delta(\epsilon - \epsilon_k) = \sum_{mn} \Lambda_{pm}^* \Lambda_{nq} \Gamma_{mn} \quad (11)$$

We define the single particle reduced density matrix (1-RDM) in the adiabatic representation as,

$$\tilde{\sigma}_{nm} = Tr_e(\hat{\rho}_{el} \hat{d}_m^\dagger \hat{d}_n) \quad (12)$$

Starting from the Liouville–von Neumann (LvN) equation,^{38,39} we derive the equation of motion (EOM) for the 1-RDM in the adiabatic representation,

$$\frac{d}{dt} \hat{\rho}_{el} = -i[\hat{H}_s, \hat{\rho}_{el}] - \hat{\mathcal{L}}_{bs} \hat{\rho}_{el}, \quad (13)$$

$$\frac{d}{dt} \tilde{\sigma}_{nm} = -i Tr_e([\hat{H}_s, \hat{\rho}_{el}] \hat{d}_m^\dagger \hat{d}_n) - Tr_e(\hat{\mathcal{L}}_{bs} \hat{\rho}_{el} \hat{d}_m^\dagger \hat{d}_n) \quad (14)$$

Following steps in Ref. 38, we can see,

$$\frac{d}{dt} \hat{\hat{\sigma}} = -i[\hat{\hat{h}}, \hat{\hat{\sigma}}] - i[U(\mathbf{R}), \hat{\hat{\sigma}}] - i[T(\mathbf{P}), \hat{\hat{\sigma}}] - \frac{1}{2}[\hat{\hat{\Gamma}}, \hat{\hat{\sigma}}]_+ + \frac{1}{2}[f(\hat{\hat{h}}), \hat{\hat{\Gamma}}]_+ \quad (15)$$

The first three terms in this equation are identical to those in Ref. 40, while the last two terms arise from the interaction between the system and the metal bath, where $f(\hat{\hat{h}})$ is the fermi function.

Without nuclear motion, the QME is

$$\frac{d}{dt} \hat{\hat{\sigma}} = -i[\hat{\hat{h}}, \hat{\hat{\sigma}}] - \frac{1}{2}[\hat{\hat{\Gamma}}, \hat{\hat{\sigma}}]_+ + \frac{1}{2}[f(\hat{\hat{h}}), \hat{\hat{\Gamma}}]_+ \quad (16)$$

and the spin current can be evaluated by

$$\begin{aligned}
I_L &= \text{Tr} \left(-\frac{1}{2} [\hat{\Gamma}_L, \hat{\sigma}]_+ + \frac{1}{2} [f_L(\hat{h}), \hat{\Gamma}_L]_+ \right), \\
I_R &= \text{Tr} \left(-\frac{1}{2} [\hat{\Gamma}_R, \hat{\sigma}]_+ + \frac{1}{2} [f_R(\hat{h}), \hat{\Gamma}_R]_+ \right), \\
I &= \frac{1}{2} (I_L + I_R)
\end{aligned} \tag{17}$$

ORBITAL SURFACE HOPPING ALGORITHM

Surface hopping (SH) is a mixed quantum-classical approach for simulating molecular dynamics. In this method, nuclear motion is treated classically, with nuclei evolving along Newtonian trajectories and their positions and velocities updated at each time step. Meanwhile, the electronic degrees of freedom are treated quantum mechanically, with the system assumed to evolve on one of several electronic potential energy surfaces (PESs) at any given moment. Given the EOM for 1-RDM above, we can derive the algorithm of orbital surface hopping for open quantum system.

Firstly, we derive the orbital quantum-classical Liouville equation (QCLE) by performing partial Wigner transformation with respect to the nuclear degree of freedoms (DOFs) on Eq. 15,

$$\begin{aligned}
\frac{d}{dt} \hat{\sigma}_W &= -i \left((\hat{h} \hat{\sigma})_W - (\hat{\sigma} \hat{h})_W \right) - i \left((U \hat{\sigma})_W - (\hat{\sigma} U)_W \right) - i \left((T \hat{\sigma})_W - (\hat{\sigma} T)_W \right) \\
&\quad - \frac{1}{2} \left((\hat{\Gamma} \hat{\sigma})_W + (\hat{\sigma} \hat{\Gamma})_W \right) + \frac{1}{2} \left((f(\hat{h}) \hat{\Gamma})_W + (\hat{\Gamma} f(\hat{h}))_W \right),
\end{aligned} \tag{18}$$

Note that the Wigner-Moyal operator can be used to express the partial Wigner transform of the product of operators \hat{A} and \hat{B} :

$$(\hat{A} \hat{B})_W = \hat{A}_W e^{-i \overleftrightarrow{\Lambda}/2} \hat{B}_W, \tag{19}$$

$$\overleftrightarrow{\Lambda} = \overleftarrow{\frac{\partial}{\partial P}} \overrightarrow{\frac{\partial}{\partial R}} - \overleftarrow{\frac{\partial}{\partial R}} \overrightarrow{\frac{\partial}{\partial P}}. \tag{20}$$

When truncating the Wigner-Moyal operator to the first order in the Taylor expansion, $e^{-i\overleftrightarrow{\Lambda}/2} \approx 1 - i\hbar\overleftrightarrow{\Lambda}/2$, we arrived at orbital QCLE,

$$\begin{aligned} \frac{d}{dt}\hat{\sigma}_W = & -i[\hat{h}_W, \hat{\sigma}_W] - \frac{P}{M} \frac{\partial \hat{\sigma}_W}{\partial R} + \frac{\partial U}{\partial R} \frac{\partial \hat{\sigma}_W}{\partial P} + \frac{1}{2} \left[\frac{\partial \hat{h}_W}{\partial R}, \frac{\partial \hat{\sigma}_W}{\partial P} \right]_+ \\ & - \frac{1}{2} [\hat{\Gamma}_W, \hat{\sigma}_W]_+ + \frac{1}{2} [f(\hat{h}_W), \hat{\Gamma}_W]_+ \end{aligned} \quad (21)$$

Note that we only keep the zeroth-order gradient expansion for the last two terms, following Ref. 39. In the orbital surface hopping, we propagate the orbital density matrix for each trajectory according to

$$\frac{d\tilde{\sigma}_{nm}}{dt} = -\frac{P}{M} \sum_l (\mathcal{D}_{nl}\tilde{\sigma}_{lm} - \tilde{\sigma}_{nl}\mathcal{D}_{lm}) - \frac{1}{2} \sum_l (\tilde{\Gamma}_{nl}\tilde{\sigma}_{lm} + \tilde{\sigma}_{nl}\tilde{\Gamma}_{lm}) + \frac{1}{2} \left(f(\tilde{h}_{nn})\tilde{\Gamma}_{nm} + \tilde{\Gamma}_{nm}f(\tilde{h}_{mm}) \right), \quad (22)$$

where \mathcal{D}_{nm} is the derivative coupling

$$\mathcal{D}_{nm} = \sum_k \Lambda_{kn}^* \frac{\partial \Lambda_{km}}{\partial R}, \quad (23)$$

For the EOM of nucleus,

$$\dot{\mathbf{R}} = \frac{\mathbf{P}}{M}, \quad (24)$$

$$\dot{\mathbf{P}} = -\frac{\partial U}{\partial \mathbf{R}} + \sum_{i=1}^n F_{\lambda_i, \lambda_i}, \quad (25)$$

where F_{λ_i, λ_i} is the force of the occupied surface λ_i .

There are two types of hopping rates: those arising from the derivative coupling within the system, denoted as $k_{n \rightarrow m}^d$, and those arising from electron transfer between the system

and the bath, denoted as k^L . For $k_{n \rightarrow m}^d$, we have

$$k_{n \rightarrow m}^d = \max \left[2\mathcal{R} \frac{P}{M} \frac{\mathcal{D}_{nm} \tilde{\sigma}_{mn}}{\tilde{\sigma}_{nn}}, 0 \right] \quad (26)$$

For the hopping rate originating from the metal surface, we only consider inter-state hopping, since the electrons on the metal surface orbitals are traced out. This implies that there is no direct hopping between the system orbitals and the bath orbitals. Consequently, each system orbital is treated as having only two possible states: occupied (denoted as 1) or unoccupied (denoted as 0). This issue has been previously resolved:^{41,42}

$$k_{nn(0 \rightarrow 1)}^L = \tilde{\Gamma}_{nn} f(\tilde{h}_{nn}), \quad (27)$$

$$k_{nn(1 \rightarrow 0)}^L = \tilde{\Gamma}_{nn} (1 - f(\tilde{h}_{nn})) \quad (28)$$

The spin current can be evaluated from Eq. 17.

We benchmarked this SH algorithm with the QME using a simple 2-level model for the system as:

$$\hat{H}_s = \begin{bmatrix} \epsilon_0 & -(t_0 + it_0) + (t_1 + it_1)(a^\dagger + a) \\ -(t_0 - it_0) + (t_1 - it_1)(a^\dagger + a) & \epsilon_0 \end{bmatrix} + \hbar\omega_0(a^\dagger a + \frac{1}{2}) \quad (29)$$

where $\epsilon_0 = -240$ meV, $t_0 = 40$ meV, $t_1 = 4$ meV, $\hbar\omega_0 = 4$ meV, while all other parameters are the same as those in Eq. 3. The quantized vibrational mode is described by bosonic creation and annihilation operators a^\dagger and a . We plot the spin current dynamics over 20 ps results both from QME (150 phonon basis) and SH (averaged over 10000 trajectories) in Fig. 10. The results show excellent agreement between the two methods, confirming the reliability of the approach presented here.

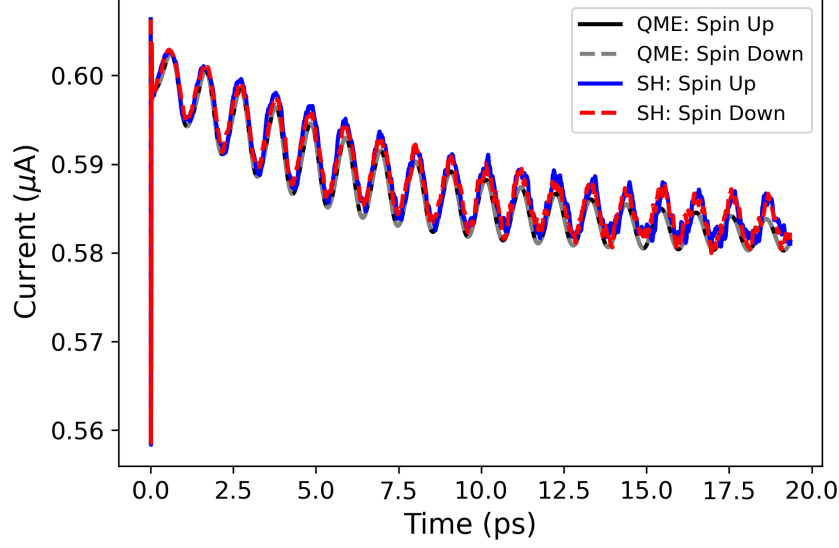


Figure 10: Time-dependent spin current for both QME and SH approaches.

ORBITAL MEAN FIELD EHRENFEST ALGORITHM

The mean-field Ehrenfest (MF) method is a mixed quantum–classical approach in which the electronic degrees of freedom are treated quantum mechanically, while the nuclei evolve classically on an averaged potential energy surface determined by the instantaneous electronic state. Therefore, the EOM of electronic density matrix is the same with that in SH algorithm (Eq. 22), while the EOM of nuclear part becomes much easier than SH:

$$\dot{\mathbf{R}} = \frac{\mathbf{P}}{M}, \quad (30)$$

$$\dot{\mathbf{P}} = Tr \left(\frac{\partial \hat{H}_s}{\partial \mathbf{R}} \hat{\sigma} \right) \quad (31)$$

CONCLUSIONS

In this work, we systematically investigated spin transport in chiral molecular junctions with and without electron–phonon coupling. Using the QME for purely electronic dynamics and SH together with MF approaches for electron–phonon interactions, we characterized the time-dependent behavior of spin current and spin polarization under varying bias voltage, molecular length, and SOC strength.

Our results demonstrate that transient spin polarization emerges within the first few hundred femtoseconds but decays to zero at long times, independent of electron–phonon coupling. Higher bias voltages increase the overall spin current but suppress spin polarization, while longer molecules and stronger SOC enhance transient polarization. Including electron–phonon coupling further modifies current–voltage characteristics, leading to current enhancement at intermediate bias but suppression at high bias, while leaving polarization dynamics largely unaffected. The SH method incorporates stochastic transitions between adiabatic potential energy surfaces, thereby providing a more accurate representation of phonon-induced broadening in transport channels, whereas the MF approach, due to its averaged mean-field character, systematically underestimates this effect.

These findings clarify the interplay of molecular length, SOC, and vibrational effects in CISS, and they emphasize the importance of considering both electronic structure and vibrational effects when designing molecular spintronic systems. Looking forward, the approaches developed here may be extended to more complex junction architectures or combined with cavity quantum electrodynamics to explore light–matter–spin interactions in chiral systems.

Acknowledgement

W.D. thanks the funding from National Natural Science Foundation of China (No. 22361142829) and Zhejiang Provincial Natural Science Foundation (No. XHD24B0301). Y.W. acknowledges supports from the National Natural Science Foundation of China No. 22403077.

References

- (1) Bloom, B. P.; Paltiel, Y.; Naaman, R.; Waldeck, D. H. Chiral induced spin selectivity. *Chemical Reviews* **2024**, *124*, 1950–1991.
- (2) Naaman, R.; Paltiel, Y.; Waldeck, D. H. Chiral molecules and the electron spin. *Nature Reviews Chemistry* **2019**, *3*, 250–260.
- (3) Ben Dor, O.; Yochelis, S.; Radko, A.; Vankayala, K.; Capua, E.; Capua, A.; Yang, S.-H.; Baczewski, L. T.; Parkin, S. S. P.; Naaman, R., et al. Magnetization switching in ferromagnets by adsorbed chiral molecules without current or external magnetic field. *Nature communications* **2017**, *8*, 14567.
- (4) Naaman, R.; Paltiel, Y.; Waldeck, D. H. Chiral induced spin selectivity gives a new twist on spin-control in chemistry. *Accounts of Chemical Research* **2020**, *53*, 2659–2667.
- (5) Firouzeh, S.; Hossain, M. A.; Cuerva, J. M.; Álvarez de Cienfuegos, L.; Pramanik, S. Chirality-induced spin selectivity in composite materials: A device perspective. *Accounts of Chemical Research* **2024**, *57*, 1478–1487.
- (6) Abendroth, J. M.; Cheung, K. M.; Stemer, D. M.; El Hadri, M. S.; Zhao, C.; Fullerton, E. E.; Weiss, P. S. Spin-dependent ionization of chiral molecular films. *Journal of the American Chemical Society* **2019**, *141*, 3863–3874.
- (7) Torres-Cavanillas, R.; Escorcia-Ariza, G.; Brotons-Alcázar, I.; Sanchis-Gual, R.; Mondal, P. C.; Rosaleny, L. E.; Giménez-Santamarina, S.; Sessolo, M.; Galbiati, M.;

- Tatay, S., et al. Reinforced room-temperature spin filtering in chiral paramagnetic metalloproteins. *Journal of the American Chemical Society* **2020**, *142*, 17572–17580.
- (8) Theiler, P. M.; Ritz, C.; Hofmann, R.; Stemmer, A. Detection of a chirality-induced spin selective quantum capacitance in α -helical peptides. *Nano Letters* **2023**, *23*, 8280–8287.
- (9) Göhler, B.; Hamelbeck, V.; Markus, T.; Kettner, M.; Hanne, G.; Vager, Z.; Naaman, R.; Zacharias, H. Spin selectivity in electron transmission through self-assembled monolayers of double-stranded DNA. *Science* **2011**, *331*, 894–897.
- (10) Alam, K. M.; Pramanik, S. Spin Filtering through Single-Wall Carbon Nanotubes Functionalized with Single-Stranded DNA. *Advanced Functional Materials* **2015**, *25*, 3210–3218.
- (11) Das, T. K.; Preyanka, N.; Mishra, S.; Sang, Y.; Fontanesi, C. Spin-Selective Anisotropic Magnetoresistance Driven by Chirality in DNA. *Advanced Functional Materials* **2025**, 2425377.
- (12) Kiran, V.; Mathew, S. P.; Cohen, S. R.; Hernández Delgado, I.; Lacour, J.; Naaman, R. Helicenes—A new class of organic spin filter. *Advanced Materials* **2016**, *28*, 1957–1962.
- (13) Qian, Q.; Ren, H.; Zhou, J.; Wan, Z.; Zhou, J.; Yan, X.; Cai, J.; Wang, P.; Li, B.; Sofer, Z., et al. Chiral molecular intercalation superlattices. *Nature* **2022**, *606*, 902–908.
- (14) Sun, R.; Park, K. S.; Comstock, A. H.; McConnell, A.; Chen, Y.-C.; Zhang, P.; Beratan, D.; You, W.; Hoffmann, A.; Yu, Z.-G., et al. Inverse chirality-induced spin selectivity effect in chiral assemblies of π -conjugated polymers. *Nature Materials* **2024**, *23*, 782–789.
- (15) Li, L.; Shi, W.; Mahajan, A.; Zhang, J.; Gómez-Gómez, M.; Labella, J.; Louie, S.; Torres, T.; Barlow, S.; Marder, S. R., et al. Too Fast for Spin Flipping: Absence

- of Chirality-Induced Spin Selectivity in Coherent Electron Transport through Single-Molecule Junctions. *Journal of the American Chemical Society* **2025**,
- (16) Evers, F.; Aharony, A.; Bar-Gill, N.; Entin-Wohlman, O.; Hedegård, P.; Hod, O.; Jelinek, P.; Kamieniarz, G.; Lemeshko, M.; Michaeli, K., et al. Theory of chirality induced spin selectivity: Progress and challenges. *Advanced Materials* **2022**, *34*, 2106629.
- (17) Yeganeh, S.; Ratner, M. A.; Medina, E.; Mujica, V. Chiral electron transport: Scattering through helical potentials. *The Journal of chemical physics* **2009**, *131*.
- (18) Eremko, A.; Loktev, V. Spin sensitive electron transmission through helical potentials. *Physical Review B—Condensed Matter and Materials Physics* **2013**, *88*, 165409.
- (19) Ghazaryan, A.; Paltiel, Y.; Lemeshko, M. Analytic model of chiral-induced spin selectivity. *The Journal of Physical Chemistry C* **2020**, *124*, 11716–11721.
- (20) Guo, A.-M.; Sun, Q.-f. Spin-selective transport of electrons in DNA double helix. *Physical review letters* **2012**, *108*, 218102.
- (21) Naskar, S.; Mujica, V.; Herrmann, C. Chiral-induced spin selectivity and non-equilibrium spin accumulation in molecules and interfaces: A first-principles study. *The Journal of Physical Chemistry Letters* **2023**, *14*, 694–701.
- (22) García-Blázquez, M. A.; Dednam, W.; Palacios, J. Nonequilibrium magnetoconductance as a manifestation of spin filtering in chiral nanojunctions. *The Journal of Physical Chemistry Letters* **2023**, *14*, 7931–7939.
- (23) Fransson, J. Chiral Induced Spin Polarized Electron Current: Origin of the Chiral Induced Spin Selectivity Effect. *The Journal of Physical Chemistry Letters* **2025**, *16*, 4346–4353.
- (24) Liu, W.; Chen, J.; Dou, W. Enhancement of chiral-induced spin selectivity via circularly polarized light. *The Journal of Physical Chemistry C* **2025**, *129*, 10181–10188.

- (25) Caetano, R. Spin-current and spin-splitting in helicoidal molecules due to spin-orbit coupling. *Scientific Reports* **2016**, *6*, 23452.
- (26) Nürenberg, D.; Zacharias, H. Evaluation of spin-flip scattering in chirality-induced spin selectivity using the Riccati equation. *Physical Chemistry Chemical Physics* **2019**, *21*, 3761–3770.
- (27) Smorka, R.; Rudge, S. L.; Thoss, M. Influence of nonequilibrium vibrational dynamics on spin selectivity in chiral molecular junctions. *The Journal of Chemical Physics* **2025**, *162*.
- (28) Fransson, J. Vibrational origin of exchange splitting and” chiral-induced spin selectivity. *Physical Review B* **2020**, *102*, 235416.
- (29) Galperin, M.; Ratner, M. A.; Nitzan, A. Molecular transport junctions: vibrational effects. *Journal of Physics: Condensed Matter* **2007**, *19*, 103201.
- (30) Mitra, A.; Aleiner, I.; Millis, A. Phonon effects in molecular transistors: Quantal and classical treatment. *Physical Review B* **2004**, *69*, 245302.
- (31) Vdovin, E. E.; Mishchenko, A.; Greenaway, M.; Zhu, M.; Ghazaryan, D.; Misra, A.; Cao, Y.; Morozov, S.; Makarovskiy, O.; Fromhold, T., et al. Phonon-assisted resonant tunneling of electrons in graphene–boron nitride transistors. *Physical review letters* **2016**, *116*, 186603.
- (32) Wang, L.; Beljonne, D. Charge transport in organic semiconductors: Assessment of the mean field theory in the hopping regime. *The Journal of Chemical Physics* **2013**, *139*.
- (33) Chen, J.; Lee, J.; Dou, W. How to correct Ehrenfest nonadiabatic dynamics in open quantum systems: Ehrenfest plus random force (E+ σ) dynamics. *The Journal of Chemical Physics* **2025**, *162*.
- (34) Reed, M. A. Inelastic electron tunneling spectroscopy. *Materials today* **2008**, *11*, 46–50.

- (35) Lorente, N.; Persson, M. Theory of single molecule vibrational spectroscopy and microscopy. *Physical review letters* **2000**, *85*, 2997.
- (36) Krause, T.; Brandes, T.; Esposito, M.; Schaller, G. Thermodynamics of the polaron master equation at finite bias. *The Journal of Chemical Physics* **2015**, *142*.
- (37) Seelig, G.; Matveev, K. Electron-phonon scattering in quantum point contacts. *Physical review letters* **2003**, *90*, 176804.
- (38) Dou, W.; Subotnik, J. E. A many-body states picture of electronic friction: The case of multiple orbitals and multiple electronic states. *The Journal of Chemical Physics* **2016**, *145*.
- (39) Dou, W.; Subotnik, J. E. A generalized surface hopping algorithm to model nonadiabatic dynamics near metal surfaces: The case of multiple electronic orbitals. *Journal of chemical theory and computation* **2017**, *13*, 2430–2439.
- (40) Ma, Y.-T.; Bi, R.-H.; Dou, W. Orbital Surface Hopping from the Orbital Quantum-Classical Liouville Equation for Nonadiabatic Dynamics of Many-Electron Systems. *Journal of Chemical Theory and Computation* **2025**, *21*, 3847–3856.
- (41) Dou, W.; Nitzan, A.; Subotnik, J. E. Surface hopping with a manifold of electronic states. II. Application to the many-body Anderson-Holstein model. *The Journal of chemical physics* **2015**, *142*, 084110.
- (42) Dou, W.; Nitzan, A.; Subotnik, J. E. Surface hopping with a manifold of electronic states. III. Transients, broadening, and the Marcus picture. *The Journal of chemical physics* **2015**, *142*, 234106.